PRESSURE DROP, FLOW DISTRIBUTION, AND TURBULENCE IN COLLECTOR HYDRAULICS

Gernot J. Pauschenwein[1], Christoph Zauner[1], Christoph Reichl[1], and Michael Monsberger[1]

[1] AIT Austrian Institute of Technology, Energy Department, Vienna (Austria)

1.   Introduction

A thorough assessment of the hydraulics of a solar thermal collector can lead to a significant amelioration of its performance. Of main interest in this context is the turbulence and hence the improved heat absorption of the collector fluid. But also the distribution of this fluid over the parallel riser pipes of the collector should be as uniform as possible (Weitbrecht et al., 2002). There are several means for the investigation of fluid flow and heat transfer in solar thermal collectors, which sometimes also depend on the collector under consideration. In this paper we focus on CFD (computational fluid dynamics) simulations in comparison to experimental results and also phenomenological 1D calculations for a particular concentrating collector (see section 3).

Very recently there have already been numerical studies on the heat transfer and fluid flow in solar thermal collectors. For example Cheng et al. (2010) used an in-house radiation modeling together with Fluent to investigate the heat transfer to a thermal oil in a parabolic-cylindrical collector (see also Kassem, 2007). Also for other types of collectors discretized numerics have been applied, e.g. to flat-plate collectors for the assessment of heat conduction to the thermal fluid in corrugated channels (Alvarez et al., 2010) and for the investigation of the complete collector physics, including radiation, air-side convection, and thermal fluid flow (Selmi et al. 2008), or to special polymer collectors with a directly radiation absorbing, black fluid (Martinopoulos et al. 2010).

Distributing the flow of the thermal fluid over the different riser tubes in a collector as equally as possible has been the focus of investigations for quite some time now (Jones and Lior, 1994), while the utilization of CFD is a quite recent phenomenon in this field. Nevertheless, the flow distribution over the riser tubes in a common U-configuration (inlet/outlet at bottom/top manifolds) has already been investigated with CFD (Fan et al., 2007, Fan and Furbo, 2008), including thermal behavior of the fluid side via a model that assumes uniform energy generation in the tube wall.

CFD as a method can be also applied to a solar thermal system on a larger scope, for example a collector in combination with a thermal storage (see e.g. Gertzos and Caouris, 2007), but our investigations focus on the collector described in the next section itself and its performance.

2.   Geometry and Conditions

The configuration of the riser and manifold pipes in the present publication is neither a Z-configuration (see e.g. Weitbrecht et al., 2002) nor a common U-configuration (see e.g. Fan and Furbo, 2008). It is what we call an Ω-configuration: The thermal fluid (in our investigations water) enters one manifold and is distributed over half of the riser pipes (in our case 5), since the manifold is blocked in the middle. In the other manifold the water is collected and again distributed over the other half of the riser pipes. It joins again in the second half of the first manifold and exits through the outlet. Fig. 4 gives a clear picture of this situation and also illustrates how a double-knee bend is attached to both the in- and outlet for construction reasons.

The standard dimensions of the involved pipes are:

- Manifold: outer diameter 15 mm, inner diameter 13.6 mm

- Riser pipes: outer diameter 8 mm, inner diameter 6.8 mm

These quantities were also subject to variations in our calculations, see section 4, in particular Fig. 9. The two manifolds are about 1 m apart while the axial distance between neighboring riser pipes is 109 mm.

The flow rate is sometimes given in terms of liters per minute per area, where area is the collector area with a

value of 2.8 m² in this case.

As mentioned the fluid entering the collector piping was water in all investigations so far, mostly at room temperature (20 °C), where the density is 998 kg/m³ and the kinematic viscosity equals 1.006 mm²/s. These properties of water were considered constant through the whole collector, i.e., the thermal influence on the fluid has not been taken into account yet. If the temperature does not vary much between in- and outlet, this is a valid approximation. It is quite exact as long as the temperature is kept roughly constant, which was the case in our comparative experiments on the test rig. The operating pressure in the pipes was 1 bar, and the inlet volume flow rate was varied up to 11.7 l/min.

3. Methods

For our experimental investigations we used the indoor test-rig for solar collector testing at AIT. The flow rate was adjusted with the help of the Coriolis measurement device ELITE from Micro Motion, and the total pressure drop between the in- and outlet (immediately after the double-knees) was measured with a LD301 SMAR pressure transmitter . To obtain the flow through each of the riser pipes in a non-invasive way the ultrasound flow measurement device FLUXUS F601 from FLEXIM was utilized.

CFD simulations were performed with Fluent. Stationary solutions were calculated with the turbulence model being k-ω SST transitional, to automatically obtain the turbulent or laminar solution, whichever happens to be the case. At the inlet a parabolic velocity profile was applied, which respects the total volume flow given as a parameter; the outlet was given a constant pressure.

In Weitbrecht et al. (2002) an analytic method for the calculation of pressure drop in pipe networks was presented, which is quite similar to what we apply here. The pressure drop along a pipe of length ℓ, also called major loss, can be calculated via the D'Arcy-Weisbach Equation

$$P_{\text{major}} = f \frac{\ell}{d_{\text{h}}} \rho \frac{u^2}{2}$$
(1)

with the average flow velocity u, the fluid density ρ, the hydraulic diameter d_{h} (equal to the diameter for circular cross sections), and the friction factor f. For laminar flow f is given by 64/Re, where Re is the Reynolds Number of the flow, while in the turbulent regime it has to be calculated through e.g. the Colebrook Equation

$$\frac{1}{\sqrt{f}} = -2.0 \lg \left(\frac{2.51}{\text{Re}\sqrt{f}} + \frac{k/d_{\text{h}}}{3.72} \right)$$
(2)

a transcendental equation in f that also contains the absolute roughness k of the pipe material. For new Copper, Lead, Brass, and Aluminum k is about 1 to 2 μm. Usually the flow is considered laminar for Re<2300 and turbulent for Re>4000, in the transition regime 2300<Re<4000 it is not well defined and depends on other factors like the inlet conditions. With a common linear interpolation in the transition regime for f the friction factor can be visualized as in Fig. 2.

For T-junctions and bends the so called minor loss is given by

$$P_{\text{minor}} = \zeta \rho \frac{u^2}{2}$$
(3)

where the minor loss coefficient ζ is dependent on the flow fractions in junctions and can be obtained e.g. from the VDI Wärmeatlas (2006). In each of the junctions of the collector harp the according pressure drops can hence be calculated as visualized in Fig. 1.

Now consider two neighboring riser pipes, 1 and 2. for a given flow distribution, the pressure drop from point A_1 of the first pipe to point E_2 of the second pipe (see again Fig. 1) can be calculated
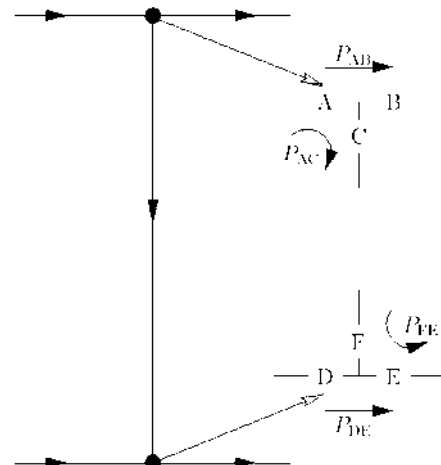

Fig. 1: Pressure drops according to Eq. (3) at the two T-junctions of one riser pipe.

along two paths: The first one is along the first riser pipe and the lower manifold (A_1-C_1-F_1-E_1-D_2-E_2) and the second one is along the upper manifold and the second riser pipe (A_1-B_1-A_2-C_2-F_2-E_2). From a physical point of view there has to be exactly one (positive) solution for the flow distribution where the pressure drops along both paths are the same.

Since the distribution also enters the calculation of the minor loss coefficients and especially the friction factor through the Reynolds number there is no way to solve for this distribution analytically. Therefore we applied an efficient method (Powell, 1964, Press et al., 1992) for finding the (vanishing) minimum of the total pressure drop discrepancies through all five paths in the 4D space of the flow distribution (the fifths flow follows from the constant total flow), i.e., we minimize the function

$$\Delta P - \sqrt{\sum_{i=1}^{n_{riser}-1} \left(\Delta P_i^{left} - \Delta P_i^{right} \right)^2}$$

(4)

where "left" and "right" correspond to the pressure drops along the two different paths (see description above).
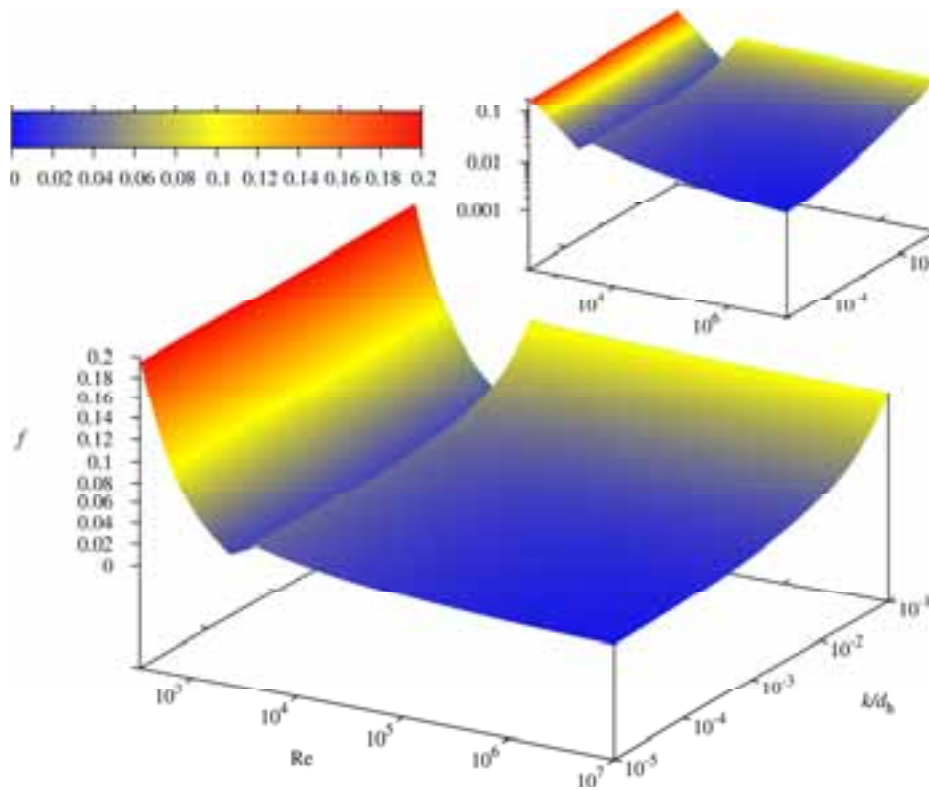

Fig. 2: The friction factor f versus Reynolds Number Re and the fraction of absolute roughness and hydraulic diameter (aka Moody Diagram). The smaller plot shows the same relation with a logarithmic f-axis.

4. Results and Comparison

The experimental result for the total pressure drop over the complete collector hydraulic system is visualized in Fig. 3 (left). The data are plotted together with the fit-function

$$\frac{\Delta P}{kPa} \quad P_0 \cdot \left(\frac{\dot{V}}{l/min} \right)^n$$

(5)

with fit-parameters P_0=0.24±0.01 and n=1.85±0.03. There are two reasons why the exponent n is not equal to 2, the expected value for turbulent flow in pipes. Firstly, at low flow rates – in the laminar regime – the pressure curve is expected to be linear, which has a decreasing effect on an overall fit-exponent. Secondly, when the flow rate is increased, the distribution of the flow over the riser pipes changes, i.e, the system can

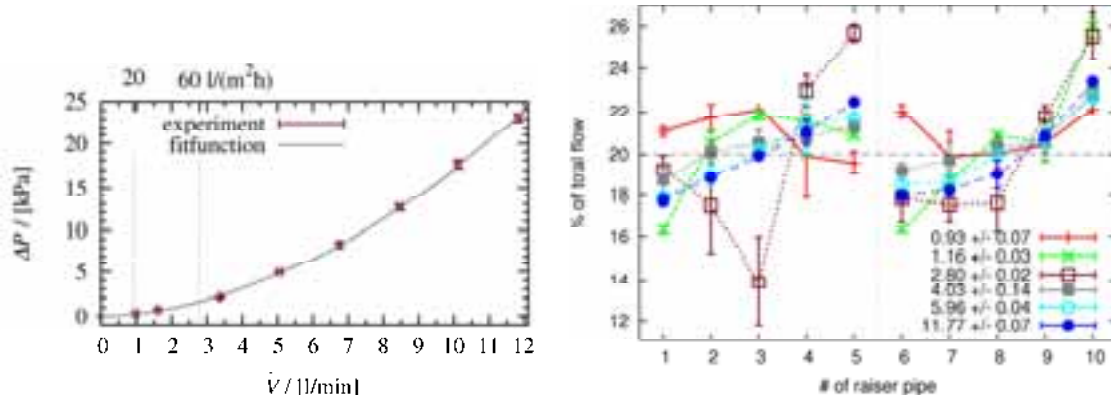partially "evade" the increasing flow resistance, leading to a smaller exponent.

Fig. 3: The total pressure drop vs. volume flow rate on the left side. The percentage of the total flow through each of the riser pipes according to the ultrasound measurement device on the right side; the vertical, dotted line indicates the change in flow direction.

As one can see in Fig. 3 on the right hand side, the ultrasound measurement device had some difficulties in determining the flow through the riser pipes, which was due to the small diameter of the pipes. The device and its data acquisition are changed and adapted to such small diameters during the time of writing; improved results will be obtained soon. Nevertheless, one can recognize a general trend: At low flow rates (red) the distribution is nearly even (note that the total sum does not add up to 1 and hence must be corrected). When turbulent phenomena kick in at an increased flow, it becomes unevenly distributed in a more or less systematic way: earlier pipes get less flow, later ones get increasingly more. This phenomenon becomes slightly reduced when turbulence is completely established.

With these experimental data as a basis the CFD calculations could be performed, an impression of its results is given in Fig. 4. The total pressure drop over the collector can be extracted from simulation data created for several volume flows and compared to the experimental results. The outcome is visualized in Fig. 5.
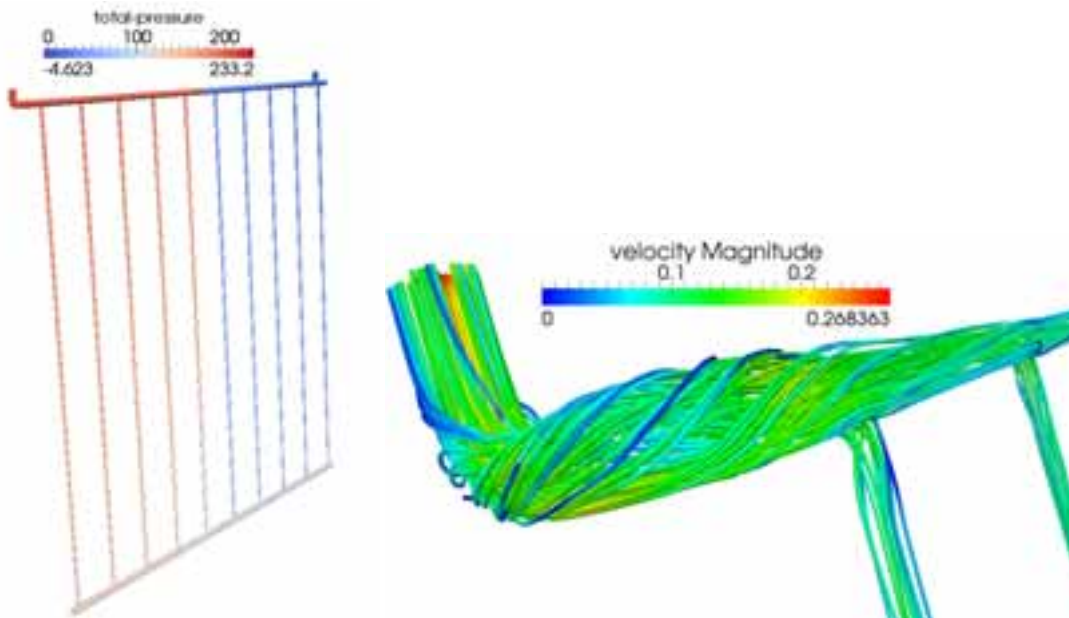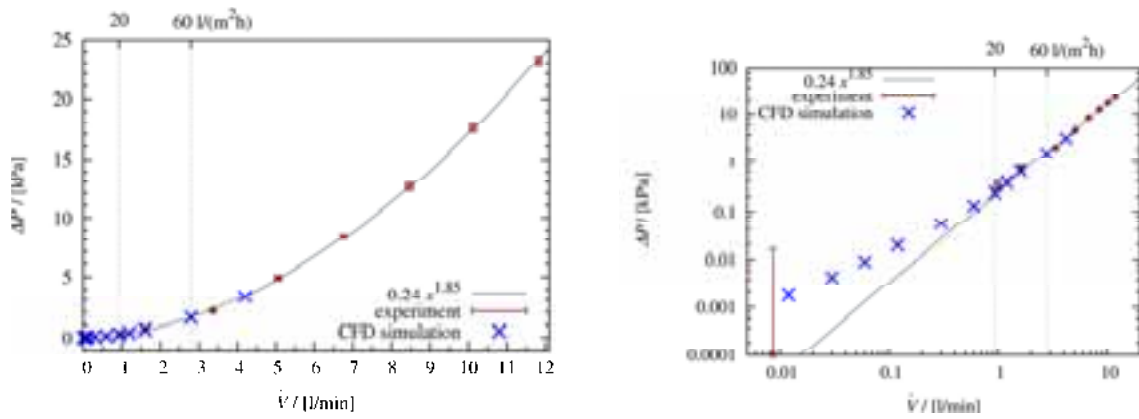

Fig. 4: Left: Total pressure drop over the collector harp in Pa. Right: Streamlines of velocity (m/s). Both pictures are taken from the case of a volume flow of 0.93 l/min.

Fig. 5: Total pressure drop versus volume flow rate from simulation and experiment (experimental fit-function also included). The right panel uses a double logarithmic scale to better visualize the low-flow regime. Volume flows that are interesting from an applicational point of view are indicated with vertical dotted lines.

One recognizes, that the experimental and CFD simulation data coincide extremely well. In the low-flow regime (below 1 l/min), which is hardly accessible experimentally, the simulation reveals what should be expected: When the flow becomes laminar, the pressure drop varies linearly with volume flow. For the experiments this phenomenon disappears within the error bars of the accuracy for the test rig and measurement series.

The pressure drop data can also be compared to the 1D-calculation results, where two considerations have to be made. Firstly, different values for the unknown effective absolute pipe roughness k have to be investigated, and secondly, a reasonable way to deal with the transition regime has to be found. In Fig. 6 the pressure drop in dependence on volume flow is depicted for four different values of k. One can see, that the method of interpolating the friction factor in the transition regime between the laminar and turbulent values at the boundaries of this regime (see Fig. 2) leads to an unfavorable, obviously wrong behavior of the curve of the pressure drop. If, on the other hand, one always chooses the larger value of the two candidates from laminar and Colebrook calculations – which means the turbulent value is used at much lower Reynolds numbers – the curves of pressure drop versus volume flow behave very much alike the experimental and CFD data. The reason for this behavior most probably is, that the bends and junctions introduce turbulence at lower flow rates (and hence smaller Reynolds numbers) where the flow could be laminar in a long, straight pipe.
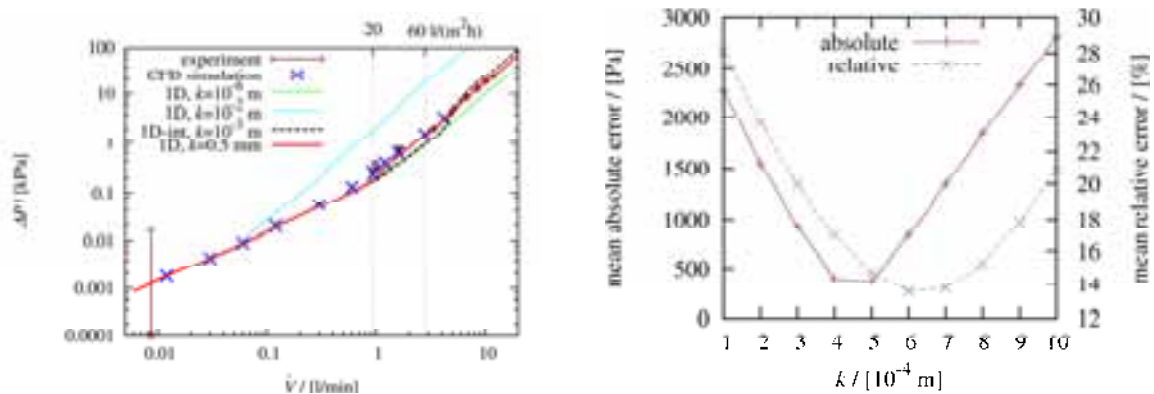
Fig. 6: Left: Pressure drop vs. volume flow from experimental, CFD, and 1D calculation data. 1D-int means the interpolation method visualized in Fig. 2 was used. Other 1D calculations favored the larger value of the friction factor. Right: The absolute and relative error between 1D calculation on the one hand and experimental and CFD data on the other hand for different values of k.

If one calculates the square root of the sum of squared differences between the 1D calculation results on the one hand and all experimental and CFD data on the other hand – in absolute as well as relative values – one finds (see Fig. 6, right), that the optimum absolute pipe roughness lies somewhere around 0.5 mm. Note however, that this is only an effective value for the complete collector harp piping which depends on but not directly represents the roughness of a particular pipe in the system.

Another instructive plot is the one of the logarithmic derivative of the pressure drop curve, motivated by the relation

$$\Delta P \propto \dot{V}^n \quad \Rightarrow \quad n \quad \frac{\mathrm{d}(\log(\Delta P))}{\mathrm{d}(\log(\dot{V}))} \tag{6}$$
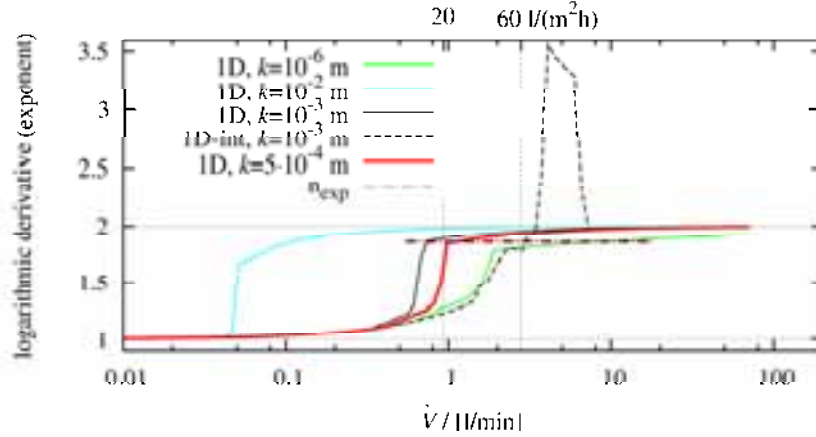
and depicted in Fig. 7.

Fig. 7: The logarithmic derivative according to Eq. (6) for the same values of k as in Fig. 6. The experimental fit for this exponent [see Eq. (5)] in the range of the experimental data is given as a dash-dotted line.

Very clearly one can see, that the potential law starts with an exponent of 1 (linear) in the low-flow, i.e., laminar regime. The smaller the roughness, the higher the volume flow at which the transition to turbulence starts, where the exponent changes from 1 to 2 (quadratic). Also, the transition regime is broader for smaller k. In addition one recognizes again, that the curve obtained with the interpolation of the friction factor (1D-int in Fig. 7) behaves quite unrealistic: The transition appears at a higher volume flow than when favoring the turbulent friction factor and an unphysical peak in the derivative is formed near the end of the transition (also compare Fig. 6, where a sharp rise is visible).

Hence we conclude that due to the "history" of the flow – entering through a double-knee and going through several T-junctions – turbulence dominates the behavior in the transition regime. Therefore, the friction factor f is best chosen to be the larger one of the laminar or Colebrook values.

The pressure drop inside the collector pipes can be directly visualized from CFD and 1D calculation data, see Fig. 8.
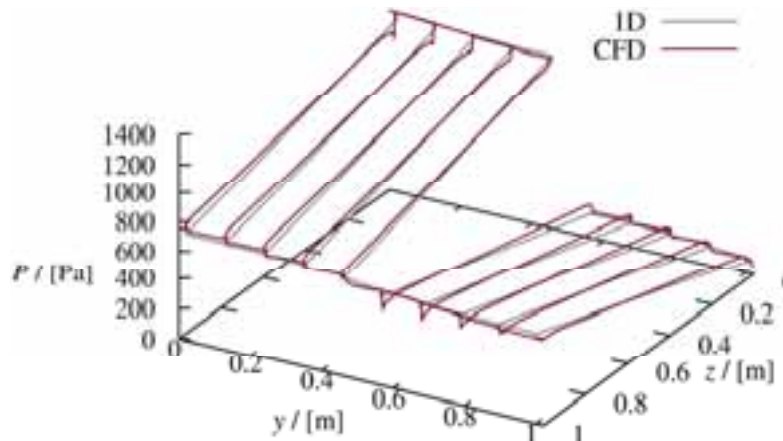

Fig. 8: Pressure drop along the pipe axes for a volume flow of 2.8 l/min from CFD simulation and 1D calculation.

Having thus verified the 1D calculations, quick investigations of diameter variations can be performed. For the manifolds pipes with outer diameters of 18, 20, 22, and 24 mm were considered (the inner diameter is always 2 mm smaller), while for the risers only one further pipe geometry was taken into account, with outer and inner diameters of 10 and 8 mm, respectively. Of course, the initial pipe geometries (see Section 2) were

also part of the parameter study.
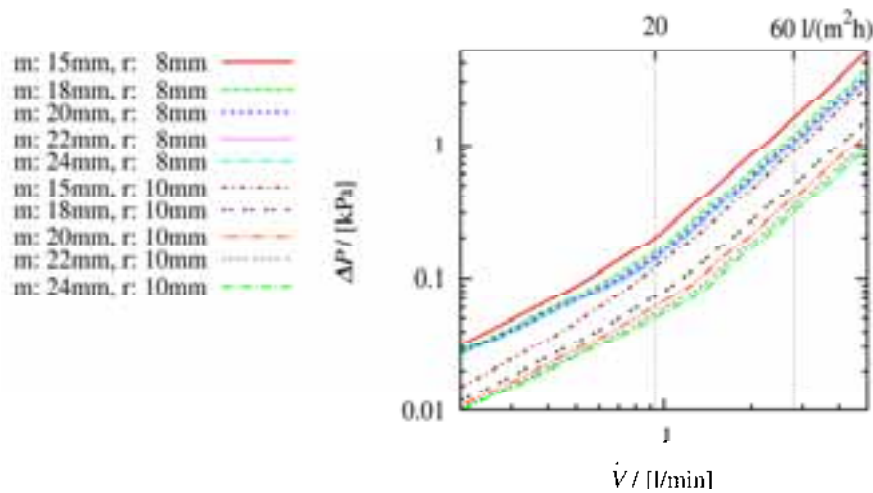
Fig. 9: Pressure drop vs. volume flow rate from 1D calculations for different combinations of manifold and riser diameters, see legend (ordered by pressure).

In Fig. 9 one can see, that the increase in riser diameter results in a much more dramatic decrease in pressure drop than an increasing manifold diameter. On the other hand, a larger riser diameter causes the transition from (overall) laminar to turbulent behavior to occur at considerably higher flow rates, while this transition regime is more or less unchanged for the considered manifold diameter variations.

Pressure drop results can also be compared to tests of collector efficiency at an average collector fluid temperature of 25 °C, see Fig. 10. It is clearly visible, that when the transition from laminar to turbulent flow occurs, the collector efficiency increases quite sharply. The second jump in efficiency, at about 3 to 4 l/min, cannot be explained by the laminar/turbulent behavior of the flow and hence the pressure drop.
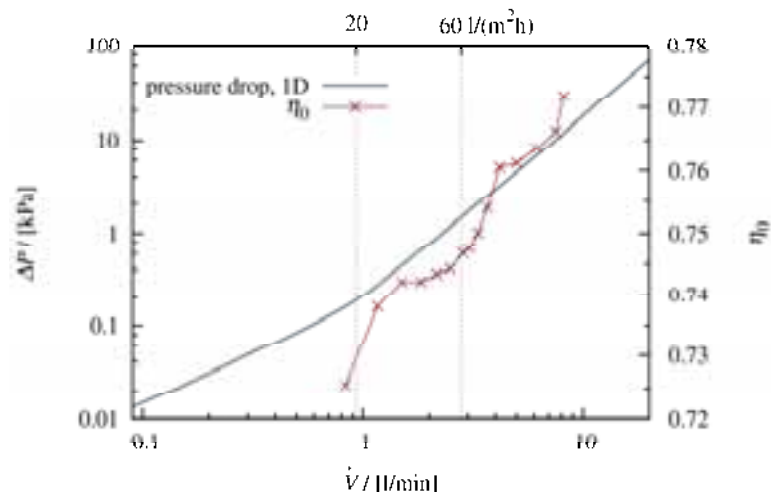
Fig 10: Pressure drop compared to collector efficiency at a fluid temperature of about room temperature.

Finally, the distribution of the volume flow over the different risers can be compared between CFD simulation and 1D calculation results. In Fig. 11 this distribution is visualized for several volume flows.

Due to the simple 1D model, the distribution between the pipes of each of the two groups of 5 pipes with the same flow direction is the same for these calculations. The CFD simulations support this model, with only one small exception at the onset of the transition regime (0,93 l/min); there, the first riser behaves slightly differently in the to and from directions, probably due to the different flow "history" (see above).

Comparing the flow distribution between CFD simulations and 1D calculations one can see, that the 1D calculations always result in a smaller deviation from the ideal average value (20%) than the simulations. This discrepancy vanishes for very slow flows (laminar regime), is largest at the transition regime and decreases again with further increasing flow rate. The general trend, i.e., which riser has less/more flow than

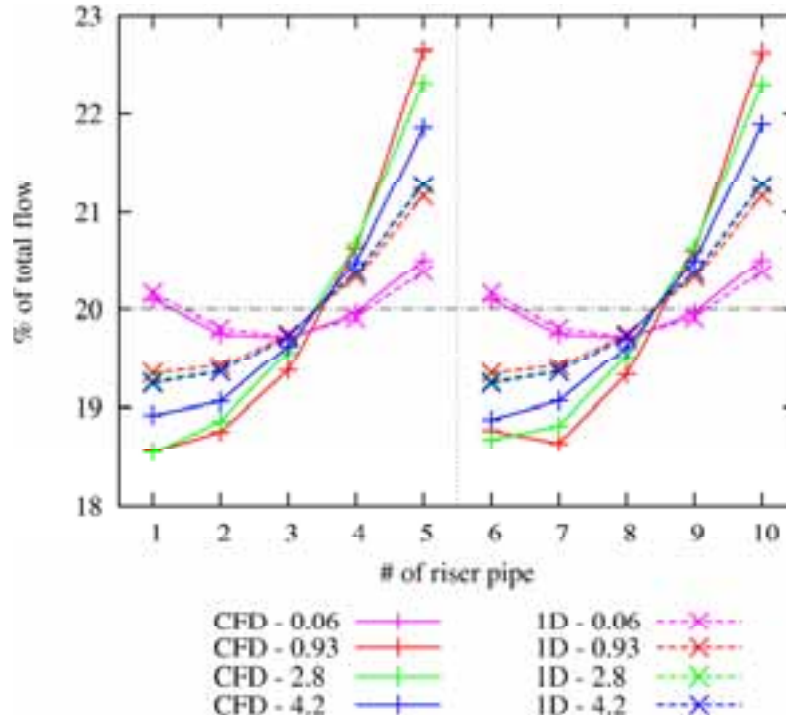the average is always correctly reflected by the calculations.

Fig. 11: Distribution of the volume flow between the 10 riser pipes of the collector at different total volume flows (indicated in the legend in l/min) from CFD simulations and 1D calculations. The vertical, dashed line separates the two parts of the collector in each of which the flow goes into the same direction.

The general trend can be described as follows:

- At very low flow rates (completely laminar regime) the flow is nearly evenly distributed across the 5 riser pipes, with only small (less than ½% of the total flow rate) deviations. These deviations result in slightly favored first and last (fifth) riser pipes.

- In the transition regime, at flow rates about 1 l/min in our example collector, the distribution becomes strongly uneven. The later the fluid reaches a riser through the manifold, the more flow enters this riser. The difference between first and last riser in one such distribution can reach even more than 4% of the total flow rate.

- Increasing the total flow rate further does not change the qualitative behavior, but the discrepancy between first and last riser decreases.

5. Outlook

Since we are investigating a solar thermal collector, it is important also to consider heat flow and temperature dependence in our experiments, simulations, and calculations. For example, the kinematic viscosity of water is higher by a factor of 2.75 at a temperature of 20 °C compared to 80 °C. Therefore the pressure drop at this higher temperature follows a different curve (see Fig. 12). In particular, the transition from laminar to turbulent flow occurs at much lower flow rates at elevated temperatures.
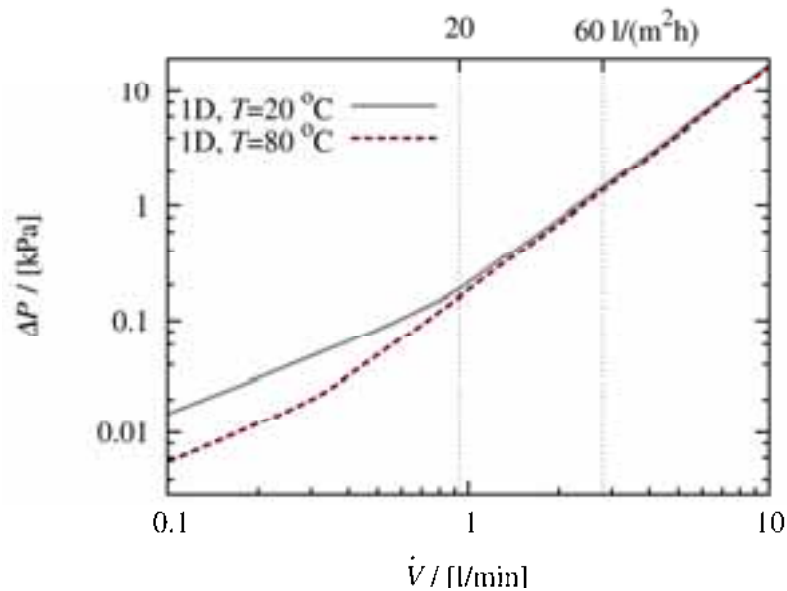
Fig. 12: Pressure drop vs. volume flow rate at two different temperatures of the water.

But not only the overall parameters can vary. When taking the heat flux through the absorber to the thermal fluid (water) into account, Temperature and hence many material parameters attain local values that have to be taken into account – a situation which is predestined to be treated with CFD. This will be the topic of our future work, a visualization of some preliminary simulations can be seen in Fig. 13.
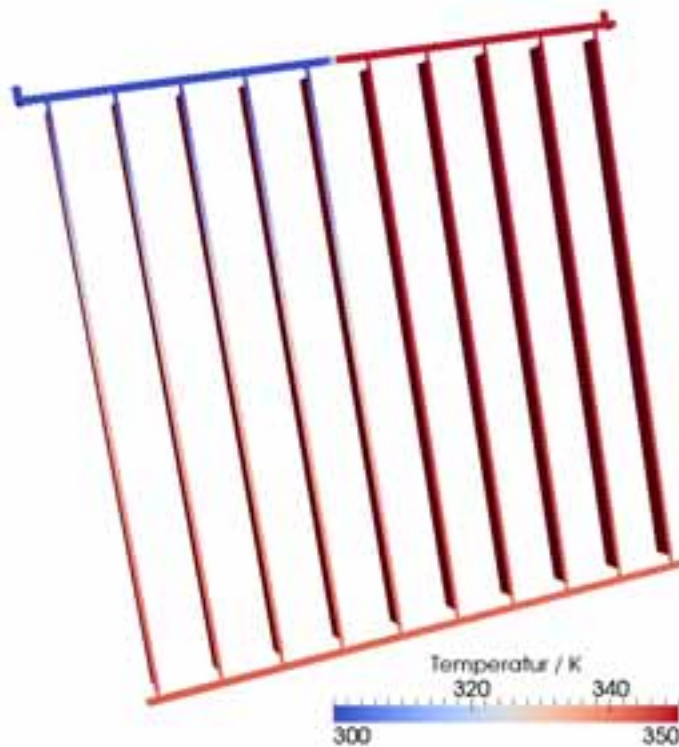

Fig. 13: Temperature distribution of the water at a constant surface temperature of 350 K (77 °C) at the absorber surface (pipes with fins).

6.   Acknowledgements

7. References

Alvarez, A.; Cabeza, O.; Muñiz, M. & Varela, L. (2010), 'Experimental and numerical investigation of a flat-plate solar collector', *Energy* **35**(9), 3707-3716.

Cheng, Z.; He, Y.; Xiao, J.; Tao, Y. & Xu, R. (2010), 'Three-dimensional numerical study of heat transfer characteristics in the receiver tube of parabolic trough solar collector', *International Communications in Heat and Mass Transfer* **37**(7), 782-787.

Fan, J.; Shah, L. J. & Furbo, S. (2007), 'Flow distribution in a solar collector panel with horizontally inclined absorber strips', *Solar Energy* **81**(12), 1501-1511.

Fan, J. & Furbo, S. (2008), 'Buoyancy Effects on Thermal Behavior of a Flat-Plate Solar Collector', *Journal of Solar Energy Engineering* **130**(2), 021010.

Gertzos, K. & Caouris, Y. (2007), 'Experimental and computational study of the developed flow field in a flat plate integrated collector storage (ICS) solar device with recirculation', *Experimental Thermal and Fluid Science* **31**(8), 1133-1145.

Jones, G. F. & Lior, N. (1994), 'Flow distribution in manifolded solar collectors with negligible buoyancy effects', *Solar Energy* **52**(3), 289-300.

Kassem, T. (2007), 'Numerical study of the natural convection process in the parabolic-cylindrical solar collector', *Desalination* **209**(1-3), 144-150.

Martinopoulos, G.; Missirlis, D.; Tsilingiridis, G.; Yakinthos, K. & Kyriakis, N. (2010), 'CFD modeling of a polymer solar collector', *Renewable Energy* **35**(7), 1499-1508.

Powell, M. J. D. (1964), 'An efficient method for finding the minimum of a function of several variables without calculating derivatives', *Comput. J.* **7**, 155-162.

Press, W.; Teukolsky, S.; Vetterling, W. & Flannery, B. (1992), *(Numerical Recipes in C)*, Cambridge University Press, Cambridge, UK.

Selmi, M.; Al-Khawaja, M. J. & Marafia, A. (2008), 'Validation of CFD simulation for flat plate solar energy collector', *Renewable Energy* **33**(3), 383-387.

VDI Wärmeatlas (2006). Publisher: Verein Deutscher Ingenieure, VDI-Gesellschaft Verfahrenstechnik und Chemieingenieurwesen (GVC), Springer.

Weitbrecht, V.; Lehmann, D. & Richter, A. (2002), 'Flow distribution in solar collectors with laminar flow conditions', *Solar Energy* **73**(6), 433-441.